




Article

High-Property Anode Catalyst Compositing Co-Based Perovskite and NiFe-Layered Double Hydroxide for Alkaline Seawater Splitting

Ruigan Hu ^{1,†}, Fuyue Liu ^{1,†}, Haoqi Qiu ¹, He Miao ^{1,*} , Qin Wang ², Houcheng Zhang ² , Fu Wang ¹ and Jinliang Yuan ¹ 

¹ Faculty of Maritime and Transportation, Ningbo University, Ningbo 315211, China; huruigan1@163.com (R.H.); liufuyue2022@163.com (F.L.); qiuhaqi1207@163.com (H.Q.); wangfu@nbu.edu.cn (F.W.); yuanjinliang@nbu.edu.cn (J.Y.)

² Department of Microelectronic Science and Engineering, Faculty of Science, Ningbo University, Ningbo 315211, China; wangqin@nbu.edu.cn (Q.W.); zhanghoucheng@nbu.edu.cn (H.Z.)

* Correspondence: miaohe@nbu.edu.cn

† These authors contributed equally to this work.

Abstract: The progress of high-efficiency non-precious metal anode catalysts for direct seawater splitting is of great importance. However, due to the slow oxygen evolution reaction (OER) kinetics, competition of chlorine evolution reaction (CIER), and corrosion of chloride ions on the anode, the direct seawater splitting faces many challenges. Herein, we develop a perovskite@NiFe layered double hydroxide composite for anode catalyst based on $\text{Ba}_{0.5}\text{Sr}_{0.5}\text{Co}_{0.8}\text{Fe}_{0.2}\text{O}_3$ (BSCF) and NiFe layered double hydroxide (NiFe-LDH) heterostructure. The optimized BSCF@CeO₂@NiFe exhibits excellent OER activity, with the potential at 100 mA cm⁻² ($E_{j=100}$) being 1.62 V in the alkaline natural seawater. Moreover, the electrolytic cell composed of BSCF@CeO₂@NiFe anode shows an excellent stability, with negligible attenuation during the long-term overall seawater splitting with the remarkable self-recovery ability in the initial operation stage, and the direct seawater splitting potential increasing by about 30 mV at 10 mA cm⁻². Our work can give a guidance for the design and preparation of anode catalysts for the direct seawater splitting.

Keywords: seawater electrolysis; perovskites; layered double hydroxide; oxygen evolution reaction; anode catalysts



Citation: Hu, R.; Liu, F.; Qiu, H.; Miao, H.; Wang, Q.; Zhang, H.; Wang, F.; Yuan, J. High-Property Anode Catalyst Compositing Co-Based Perovskite and NiFe-Layered Double Hydroxide for Alkaline Seawater Splitting. *Processes* **2022**, *10*, 668. <https://doi.org/10.3390/pr10040668>

Academic Editor: Mingxia Gao

Received: 1 March 2022

Accepted: 27 March 2022

Published: 29 March 2022

Publisher's Note: MDPI stays neutral with regard to jurisdictional claims in published maps and institutional affiliations.



Copyright: © 2022 by the authors. Licensee MDPI, Basel, Switzerland. This article is an open access article distributed under the terms and conditions of the Creative Commons Attribution (CC BY) license (<https://creativecommons.org/licenses/by/4.0/>).

1. Introduction

Hydrogen with high energy density (142 MJ kg⁻¹) and clean nature can hold great significance for “carbon neutrality” and has been widely hypothesized to be the most promising sustainable energy in the future [1–5]. Using intermittent clean energies such as wind energy and solar energy to split fresh water is well considered as one of the most sustainable H₂ production technologies [6]. Generally, water splitting (2H₂O + energy → 2H₂ + O₂) consists of two half-reactions, the oxygen evolution reaction (OER) on the anode side and the hydrogen evolution reaction (HER) on the cathode side. The kinetic process of OER is much slower than that of HER due to the fact that the former involves a complicated four-electron transfer, while the latter only involves two-electron transfer [7–9]. Therefore, the OER performance of the anode is critical to the water splitting efficiency.

Compared with fresh water, seawater occupying about 97% of the Earth's water resources is inexhaustible [10]. Therefore, splitting seawater to produce H₂ instead of fresh water has received more and more attention due to the following facts [11,12]. Firstly, seawater is a very abundant resource on our planet compared with the scarce freshwater resources [11]. Secondly, the direct seawater splitting without desalination can simplify electrolysis systems by eliminating the complex desalination equipment [13]. Finally, the direct seawater splitting is of

great importance. However, the direct seawater splitting faces many challenges, especially for the anode sides [3]. The biggest challenges for direct seawater splitting are the chlorine evolution reaction (CER, $2\text{Cl}^- \rightarrow \text{Cl}_2 + 2\text{e}^-$, $E^0 = 1.36 \text{ V}$ vs. reversible hydrogen electrode (RHE)) and the corrosion of chloride ions on anode electrocatalysts. It is well known that the chloride ion content in seawater is about 0.5 M [14], and its oxidation to form Cl_2 involves only a two-electron/proton transfer process, which will compete with OER on the anode side. Under alkaline conditions ($\text{pH} > 7.5$), the equilibrium potential of CER ($2\text{Cl}^- \rightarrow \text{Cl}_2 + 2\text{e}^-$, $\text{Cl}_2 + 2\text{OH}^- \rightarrow \text{OCl}^- + \text{H}_2\text{O}$, $E^0 = 1.72 \text{ V}_{\text{RHE}}$) is large, being about 490 mV higher than that of OER (1.23 V vs. RHE) [15]. The Cl_2 produced by CER in the alkaline medium will further combine with the OH^- in the electrolyte to form hypochlorite, which aggravates the corrosion on the anode catalyst. In addition, during the direct splitting of seawater to produce hydrogen [15], the bacteria, microorganisms, suspended solid particles, and some metal ions (such as Mg^{2+} , Ca^{2+} , etc.) that can easily form hydroxide precipitation ($\text{M}^{2+, x+} + \text{OH}^- \rightarrow \text{M}(\text{OH})_{2, x}$, $\text{M} = \text{Mg}^{2+}$, Ca^{2+} , etc.) also have serious impacts on OER catalysts. Therefore, direct seawater splitting should follow several conditions: (1) adopting alkaline electrolyte to suppress CER; (2) the anode voltage below 1.72 V (vs. RHE) to avoid the generation of ClO^- and ensure an approximative 100% OER; and (3) the electrodes on both sides have good activity, selectivity, corrosion resistance, and durability.

Recently, some high-efficiency non-precious metal catalysts including transition metal oxides [16–22], nitrides [1,23,24], phosphides [25,26], sulfides [27–30], and (oxy)hydroxides [31–34], etc. have been developed for seawater splitting. Among them, NiFe-layered double hydroxide (NiFe-LDH) have great advantages of a low cost, facile synthesis process and superior OER activity [15]. Nevertheless, the OER activity of NiFe-LDH degrades rapidly at high current densities ($j > 100 \text{ mA cm}^{-2}$), and few NiFe-LDH catalysts can retain 80% of their initial current density after 24 h in seawater [35]. Hence, its stability needs to be further improved for practical seawater splitting [36].

In the past few years, some Co-based perovskites with excellent OER activities and stabilities have been exploited as anode catalysts for water oxidation [37–40]. Among these Co-based perovskites, $\text{Ba}_{0.5}\text{Sr}_{0.5}\text{Co}_{0.8}\text{Fe}_{0.2}\text{O}_3$ (BSCF) even shows an acceptable OER catalytic activity compared with the state-of-the-art iridium and ruthenium dioxides (IrO_2 and RuO_2) [27,41]. The latest work indicates that the compositing cerium oxide (CeO_2) can significantly improve the OER catalytic properties of some metal compounds such as LaFeO_3 [42], RuO_2 [43], and NiMn-LDH [44]. CeO_2 has a strong oxygen accumulation ability and lots of oxygen vacancies [45], and its (111) facet can promote OER catalysis. Therefore, it is easy to assume that compositing NiFe-LDH, CeO_2 with BSCF can construct a robust anode catalyst with good OER performances for seawater splitting.

Herein, we synthesized a novel compositing anode catalyst of BSCF@ CeO_2 @NiFe with a heterogeneous structure by a facile precipitation method. The BSCF@ CeO_2 @NiFe catalyst exhibits much higher OER activity (with $E_{j=100} = 1.52 \text{ V}$ vs. RHE) than that of NiFe-LDH in alkaline medium. Moreover, our BSCF@ CeO_2 @NiFe has high durability in the alkaline natural seawater, suggesting that it can be used as a promising candidate for seawater splitting.

2. Materials and Methods

2.1. Synthesis of Materials

All the reagents mentioned in this work were analytical grade (AR) and purchased from commercial channels without further processing unless otherwise specified. The classic sol-gel method was adopted to synthesize the $\text{Ba}_{0.5}\text{Sr}_{0.5}\text{Co}_{0.8}\text{Fe}_{0.2}\text{O}_3$ (BSCF) according to our previous work [46]. The stoichiometric ratio of $\text{Co}(\text{NO}_3)_2 \cdot 6\text{H}_2\text{O}$, $\text{Fe}(\text{NO}_3)_3 \cdot 9\text{H}_2\text{O}$, $\text{Ba}(\text{NO}_3)_2$ and $\text{Sr}(\text{NO}_3)_2$ (Sinopharm Chemical Reagent Co., Ltd. Ningbo, China) were dissolved into 250 mL deionized (DI) water followed by adding citric acid (CA) and ethylenediaminetetraacetic acid (EDTA, Aladdin Ltd., Shanghai, China). The total mole of metal ions:CA:EDTA = 1:1.5:1, and the pH value of the mixture was adjusted to about

6 with $\text{NH}_3 \cdot \text{H}_2\text{O}$. Then, the mixture was vigorously stirred at a temperature of $80\text{ }^\circ\text{C}$. After the gel formed, it was placed at $180\text{ }^\circ\text{C}$ and kept for 10 h in air. Subsequently, the dry gel was sintered at $950\text{ }^\circ\text{C}$ for 5 h, and its heating rate was $100\text{ }^\circ\text{C h}^{-1}$. Finally, the obtained powder was further ball-milled for 1 h to obtain BSCF.

The subsequent loading of CeO_2 on BSCF are synthesized by a precipitation method. For synthesizing BSCF@CeO_2 , 1 mmol (0.218 g) BSCF was dispersed in 1 mL ethanol, then 100 mL DI water was added with continuous stirring at room temperature. Then, 100 mL 0.060 wt % cationic polyacrylamide (CPAM, 0.060 g, Baichuan Biotechnology Co., Ltd., Ningbo, China) clear solution was slowly added to pretreat the BSCF powder for 1 h. Afterwards, the product was centrifuged, filtered, and then placed in 100 mL of DI water and heated at $50\text{ }^\circ\text{C}$. Next, 1 mmol $\text{Ce}(\text{NO}_3)_2 \cdot 6\text{H}_2\text{O}$ and 3.2 mmol NaOH (Sinopharm Chemical Reagent Co., Ltd., Ningbo, China) was dissolved in 100 mL DI water, respectively. Then, two solutions were slowly dripped into the above mentioned BSCF–water mixture and the solution pH value kept at 9.5 during the whole process. Next, the precipitated product was centrifuged and filtered for three times with DI water and ethanol, and then dried at $100\text{ }^\circ\text{C}$ for 10 h. Finally, the above dried product was heated to $600\text{ }^\circ\text{C}$ for 2 h in order to yield the product of BSCF@CeO_2 -11. It should be noted that the former “1” represented the total moles of BSCF, and the latter “1” represented the total moles of added cerium ions. For comparison, a similar method was adopted to prepare the CeO_2 except for the use of BSCF and CPAM.

The subsequent loading of NiFe-LDH on BSCF@CeO_2 are synthesized by a precipitation method. For synthesis of $\text{BSCF@CeO}_2\text{@NiFe}$, 0.1 g BSCF@CeO_2 -11 was placed into 100 mL DI water and maintained a constant stirring at ambient temperature. We dissolved a certain amount of $\text{Ni}(\text{NO}_3)_2 \cdot 6\text{H}_2\text{O}$ and $\text{Fe}(\text{NO}_3)_3 \cdot 9\text{H}_2\text{O}$ (Ni:Fe = 3:1) into 100 mL DI water, then dissolved a certain amount of NaOH and Na_2CO_3 (Sinopharm Chemical Reagent Co., Ltd., Ningbo, China) into another 100 mL DI water, and kept the solutions at $[\text{OH}^-] = 1.6 \times [\text{Ni}^{2+} + \text{Fe}^{3+}]$, $[\text{CO}_3^{2-}] = 2.0 \times [\text{Fe}^{3+}]$ [47]. Then, we slowly dripped the above two solutions into the solution containing BSCF@CeO_2 at the same time, maintaining the pH value of 9.5, and stirring for 2 h during the whole process. Ultimately, the product was centrifuged, filtered, and evaporated at $80\text{ }^\circ\text{C}$ for 10 h to yield the product of $\text{BSCF@CeO}_2\text{@NiFe}$. In order to probe the loading effect on the OER properties, we loaded NiFe-LDH (Ni:Fe = 3:1) with total moles fraction of 2.0, 3.0, 4.0, and 6.0 mmol on BSCF@CeO_2 , and abbreviated as $\text{BSCF@CeO}_2\text{@NiFe-11x}$ ($x = 2, 3, 4, 6$), respectively. For comparison, a similar method was adopted to prepare the NiFe-LDH except for the use of BSCF@CeO_2 and stirring at $50\text{ }^\circ\text{C}$ for 6 h [48].

2.2. Material Characterizations

X-ray diffraction (XRD) patterns were fetched on a Bruker D8 Advance X-ray diffractometer ($\text{Cu K}\alpha = 1.5418\text{ \AA}$, Bruker Ltd., Karlsruhe, Germany) at a scanning rate of 0.02° s^{-1} from 20° to 90° . The micromorphology of the synthesized samples was observed by using a field-emission scanning electron microscopy (SEM, Hitachi S4800, 5 kV, Hitachi Ltd., Tokyo, Japan).

2.3. Electrochemical Measurements

The preparation method of the catalyst ink was described as the following according to our previous work [49]: 5 mg catalyst and 5 mg carbon (Vulcan-XC72, Cabot Ltd., Shanghai, China) were dispersed in 2.0 mL ethanol plus 80 μL of 5 wt% Nafion (DuPont Ltd., Beijing, China) solution and ultrasonically blended for 2 h to form a well-dispersed ink. Then, 20 μL of the ink was pipetted on a polished glassy carbon (GC) electrode for preparation of working electrode, and the solvent was evaporated naturally with a catalyst loading of $\sim 0.245\text{ mg cm}^{-2}$. For measuring the working electrode, oxygen with ultrahigh purity grade was bubbled into the electrolyte to make it O_2 -saturated during the measurements so as to guarantee the $\text{O}_2/\text{H}_2\text{O}$ equilibrium at 1.23 V vs. RHE. The standard three-electrode system (the above working electrode, the counter electrode of carbon rod, and the reference

electrode of Hg/HgO (1 M NaOH) electrode), rotating disc electrode (RDE, PINE) and the electrochemical performances of the above specimens were recorded by CHI 760E electrochemical workstation (Shanghai Chenhua, China) in 1 M KOH under a rotating speed of 1600 rpm.

Before the electrochemical test, several cyclic voltammetry (CV) scans (0.2~1.0 V vs. Hg/HgO) were performed to remove the bubbles covered on the catalysts. Linear sweep voltammetry (LSV) was recorded from 0.2 to 1.0 V vs. Hg/HgO at a scan rate of 5 mV s⁻¹. Electrochemical impedance spectrum (EIS) was measured at 1.676 V vs. RHE over a frequency range from 10⁶ to 1 Hz. The equation: $\eta = E_{\text{RHE}} - 1.23 \text{ V}$ was adopted to work out the overpotentials (η) of the working electrodes, and the Tafel equation: $\eta = b \log j + a$ was adopted to work out Tafel slopes, where η is the overpotential, j represents current density, and b is the Tafel slope [50]. The electrochemically active surface area (ECSA = C_{dl}/C_s) was assessed by measuring double-layer capacitance (C_{dl}) from CV with different scanning rates. C_s represents the specific capacitance of 1.0 M KOH (0.04 mF/cm²) [50]. The C_{dl} which was positively correlated to the ECSA was assessed by $C_{\text{dl}} = j_c/V$, where j_c represented the current density, and V was the voltage measured by CV. The scanning potential range was from 0.15 to 0.25 V (vs. Hg/HgO). The measured potentials were transformed to potentials vs. RHE by the Nernst equation ($E_{(\text{RHE})} = E_{(\text{Hg}/\text{HgO})} + 0.098 + 0.059 \times \text{pH}$). In addition, the equation ($E_c = E_M - iR_s$) was adopted to correct the compensated potential, where R_s is the ohmic solution resistance measured by EIS, i is the current, E_c is the correction voltage and E_M is the measurement voltage. The stability tests of the catalysts were performed by the continuous LSV and CV scanning.

The anodes for overall water (alkaline water, alkaline simulated seawater, and alkaline natural seawater) splitting (OWS) were composed of the as-prepared catalyst and RuO₂ ink drip-coated on Ni foam (NF, 1 cm × 1 cm, Sinero Co., Ltd., Beijing, China) with the total load being about 4.0 mg cm⁻². The cathode was commercial 20 wt% Pt/C (Aladdin Ltd., Cardiff, UK) which was dripped onto NF with the total load of about 2.0 mg cm⁻². The stability tests of OWS were performed at 100 mA cm⁻² for alkaline aqueous solution and alkaline simulated seawater [51] (seeing Table S1, Supplementary Information), but 10 mA cm⁻² for alkaline natural seawater (taken from the East China Sea, 29°52'00.00" N, 121°31'00.00" E). All the OWS stability tests were uncompensated for resistance. In our work, the simulation seawater in our paper is 0.5 M NaCl solution. The alkaline nature seawater in our paper indicates the mixed solution of nature seawater with 1 M KOH.

3. Results

Figure 1a shows the simple precipitation synthesis process of BSCF@CeO₂@NiFe. The micromorphology of the different catalysts is observed by SEM. As shown in Figure 1b, the BSCF powder particles with a relatively smooth surface are very large, with the diameter >1 μm. The surface of BSCF@CeO₂ (Figure 1d) is very rough due to a large number of fine CeO₂ particles with the diameter of about tens of nanometers coated on the BSCF surface. BSCF@CeO₂@NiFe shows a similar morphology with BSCF@CeO₂, while some NiFe-LDH nanorods entangled with the CeO₂ nanoparticles can be found on the BSCF surface (Figure 1e). In addition, BSCF@NiFe almost shows the same micromorphology with BSCF@CeO₂@NiFe (Figure 1c).

Figure 1f shows the XRD patterns of BSCF@CeO₂@NiFe, BSCF@NiFe, NiFe-LDH, BSCF@CeO₂, BSCF, and CeO₂. It is obvious that the XRD peaks of BSCF@CeO₂@NiFe correspond with BSCF (PDF#01-075-6980, space group Pm-3m), CeO₂ (PDF#43-1002, space group Fm-3m), and NiFe-LDH (PDF#00-040-0215, space group R-3m), and no other impurity phases can be found. It is worth noting that Sr ions in A-site of BSCF is easy to segregate during sintering and electrochemical processes [52,53], and then deteriorate the stability of the BSCF crystal structure. When BSCF is directly contacted with alkaline solution, especially carbonate solution, A-site ions (Ba²⁺ and Sr²⁺) are easy to form carbonates (Sr_{0.8}Ba_{0.2}CO₃) (Figure 1g) due to the electronegative nature of BSCF surface [54]. Therefore, during the synthesizing process of BSCF@CeO₂, it is essential to coat the organic

compound (CPAM) containing cationic characteristics on the BSCF surface to reduce the electronegativity [54]. By introduction of CPAM, the impurity phase of $\text{Sr}_{0.8}\text{Ba}_{0.2}\text{CO}_3$ can be effectively prevented.

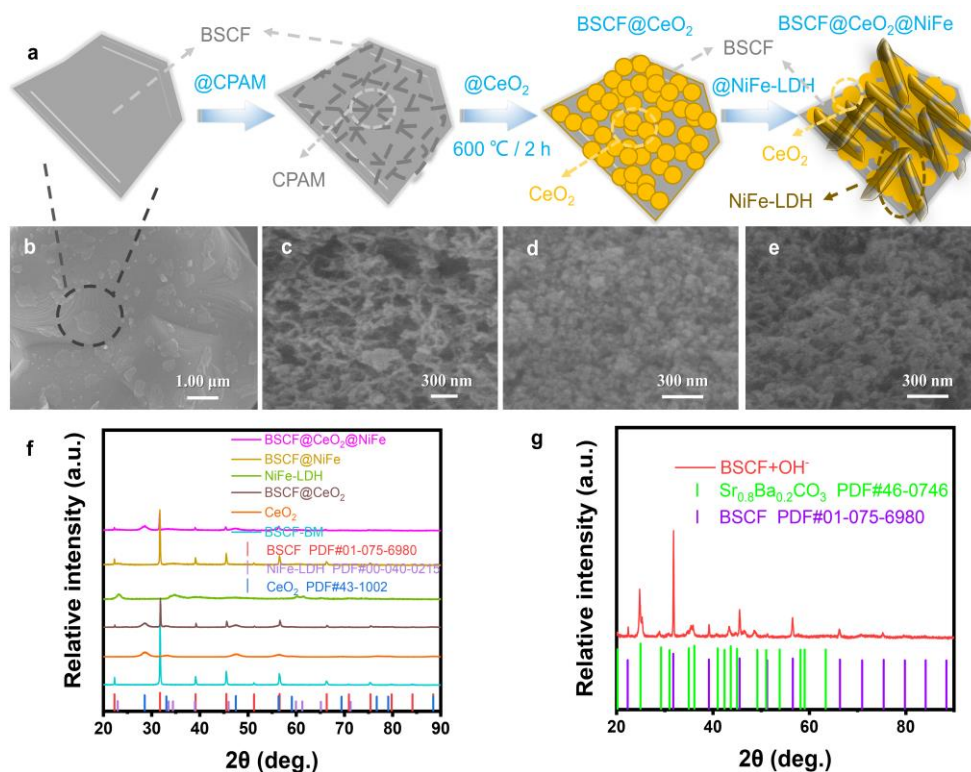


Figure 1. (a) Schematics of the preparation of BSCF@CeO₂@NiFe. SEM images of BSCF (b), BSCF@NiFe (c), BSCF@CeO₂ (d), and BSCF@CeO₂@NiFe (e). (f) XRD patterns of BSCF@CeO₂@NiFe, BSCF@NiFe, NiFe-LDH, BSCF@CeO₂, BSCF and CeO₂. (g) XRD pattern of BSCF soaked in alkaline solution containing CO_3^{2-} after 2 h.

The OER LSV curves of the different catalysts are measured to evaluate their catalytic activities. BSCF perovskite as a classic oxygen evolution reaction (OER) catalyst, has an excellent intrinsic catalytic activity compared with other perovskites [55]. As shown in Table S2, the OER potential of BSCF at 10 and 100 mA cm^{-2} are much lower than those of most perovskites. However, the HER activity of BSCF is very poor, and it cannot be used as a cathode catalyst for direct seawater splitting (Figure S1, Supplementary Information). In order to optimize the composition of BSCF@CeO₂@NiFe composite catalysts, we measure the OER catalytic activities of BSCF@CeO₂@NiFe-11x ($x = 2, 3, 4, 6$) in 1M KOH alkaline solution. Obviously, BSCF@CeO₂@NiFe-113 has the highest OER performance among these samples (Figure 2a) and can be used as a follow-up research object (abbreviated as BSCF@CeO₂@NiFe). Moreover, compared with BSCF@NiFe, BSCF@CeO₂, and BSCF, BSCF@CeO₂@NiFe has the much lower overpotential of 297 mV at 100 mA cm^{-2} , which is even lower than that of NiFe-LDH (315 mV) and RuO₂ (344 mV) (Figure 2b,c). Additionally, BSCF@CeO₂@NiFe owns the smallest Tafel slope of 56.0 mV dec^{-1} among above four samples (Figure 2d), which indicates its superior OER catalytic kinetics. From Figure 2e and Table S3, it is obvious that the OER activity of our catalyst is almost the highest among those of the previously reported perovskites and NiFe-LDH catalysts.

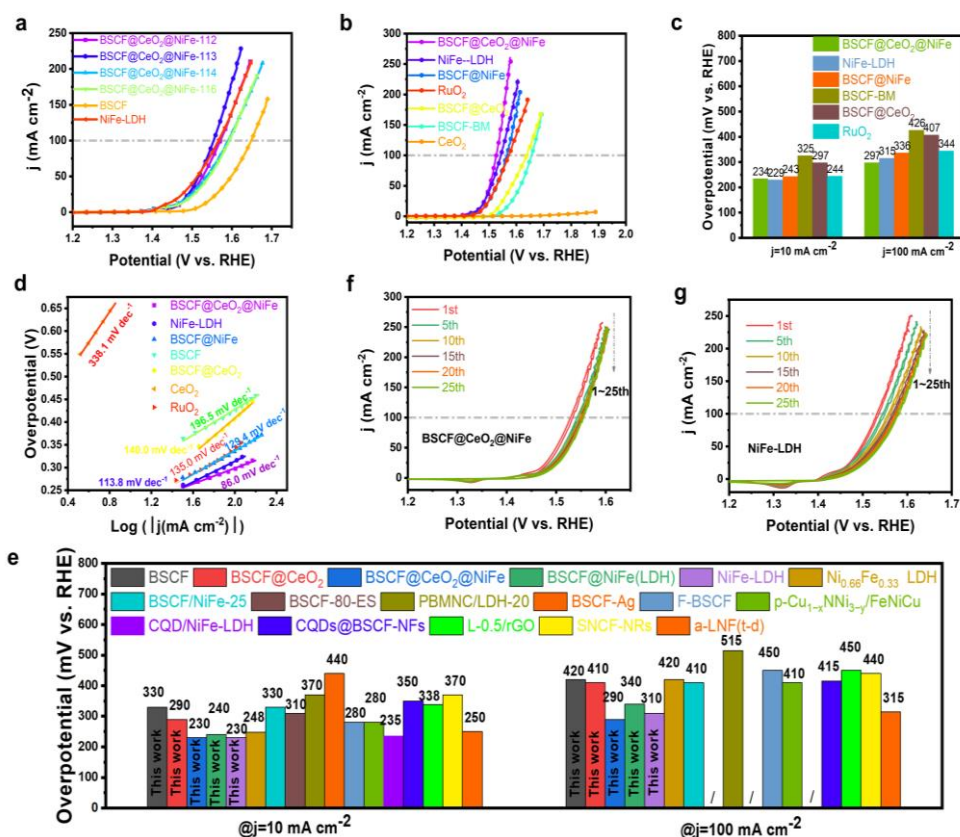


Figure 2. OER LSV curves of (a) the BSCF@CeO₂@NiFe-LDH with the different compositions and (b) BSCF@CeO₂@NiFe, BSCF@NiFe, NiFe-LDH, BSCF@CeO₂, BSCF, CeO₂, and RuO₂ in 1 M KOH solution. (c) Corresponding overpotentials at 10 and 100 mA cm⁻², (d) Tafel plots. CV curves of BSCF@CeO₂@NiFe. (e) Comparison of the OER activities of the different type of composite perovskites in this work and the other reports, and (f) NiFe-LDH (g) at the different scanning circles in 1 M KOH solution.

Although NiFe-LDH has an excellent OER catalytic activity, its stability needs to be further improved (seeing Figure S2, Supplementary Information) [36]. The stabilities of BSCF@CeO₂@NiFe and NiFe-LDH are performed by 25-cycle CV scans (Figure 2f,g and Figure S3). The result shows that the potential of BSCF@CeO₂@NiFe slightly increases from 1.52 to 1.55 V at 100 mA cm⁻² after 25-cycle CV scanning, whereas the potential of NiFe-LDH increases from 1.53 to 1.58 V at 100 mA cm⁻² after the same CV scanning cycles. Compared with NiFe-LDH, the high stability of BSCF@CeO₂@NiFe can be attributed to the synergistic effect of BSCF [56] and NiFe-LDH.

Subsequently, we explore the OWS properties of BSCF@CeO₂@NiFe. As shown in Figure 3a, the OER catalytic activities of BSCF@CeO₂@NiFe are measured in 1 M KOH, 1 M KOH + 0.5 M NaCl, and 1 M KOH + seawater on RDE. The results show that the OER catalytic activities of BSCF@CeO₂@NiFe in 1 M KOH and 1 M KOH + 0.5 M NaCl solutions are very close, while the OER catalytic activity of BSCF@CeO₂@NiFe is far lower in 1 M KOH + seawater, compared with that in 1 M KOH. This can correspond to the fact that the bacteria, microorganisms, suspended solid particles, and some metal ions have serious impacts on the OER catalysts. Furthermore, we assemble an electrolytic cell with BSCF@CeO₂@NiFe anode and 20 wt% Pt/C cathode (Figure 3b) to study the OWS performances of BSCF@CeO₂@NiFe anode in 1 M KOH, 1 M KOH + 0.5 M NaCl, and 1 M KOH + seawater. As shown in Figure 3b, the OWS potentials of the electrolytic cell with BSCF@CeO₂@NiFe are 1.69 V and 1.70 V at 100 mA cm⁻² in 1 M KOH and 1 M KOH + 0.5 M NaCl, respectively, which is even lower than that with RuO₂ (1.74 V in 1 M KOH). In addition, the OWS potential of the electrolytic cell at 100 mA cm⁻² in

1 M KOH + seawater is as large as 1.76 V, corresponding to the OER catalytic activity of BSCF@CeO₂@NiFe in the alkaline natural seawater.

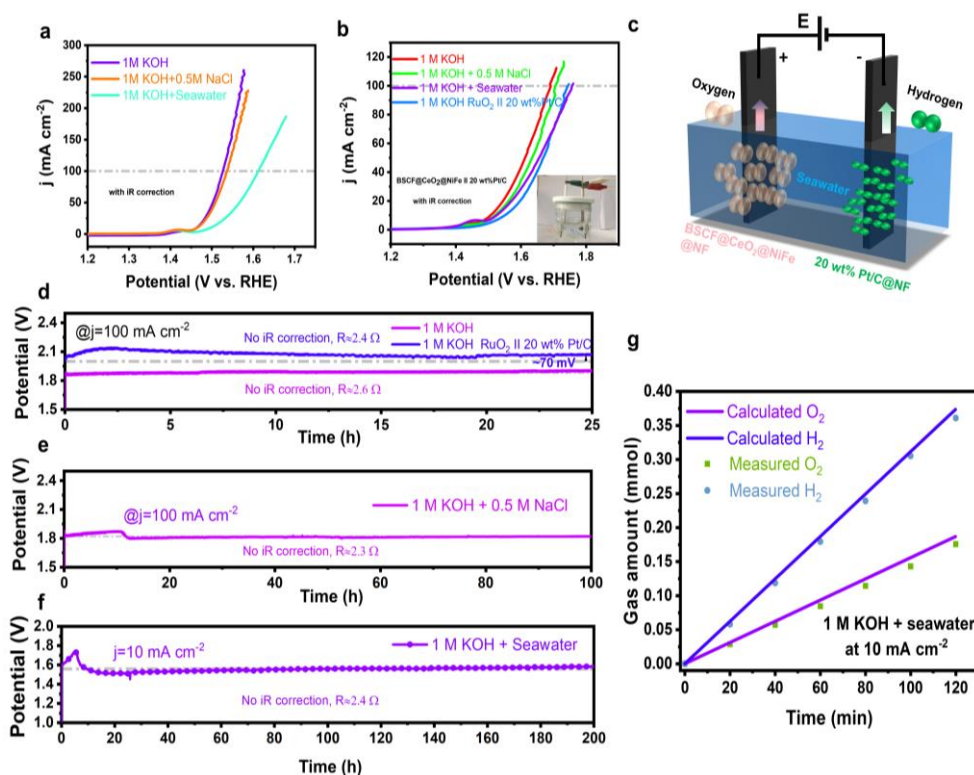


Figure 3. (a) OER LSV curves of BSCF@CeO₂@NiFe and (b) polarization curves of overall water splitting with BSCF@CeO₂@NiFe anode in 1 M KOH (and RuO₂), 1 M KOH + 0.5 M NaCl, and 1 M KOH + seawater. Insert of (b) is the illustration of overall water splitting. (c) Schematics of overall seawater splitting. (d) Stabilities of BSCF@CeO₂@NiFe and RuO₂ anodes for overall water splitting in 1 M KOH, (e) 1 M KOH + 0.5 M NaCl, and (f) 1 M KOH + seawater. (g) Faradaic efficiency measurement in 1 M KOH + seawater at 10 mA cm⁻².

In order to estimate the OWS stability, we measure the voltage vs. time curves of BSCF@CeO₂@NiFe in 1 M KOH (Figure 3d) and 1 M KOH + 0.5 M NaCl (Figure 3e) at 100 mA cm⁻². Figure 3d shows that the voltage of the electrolytic cell with BSCF@CeO₂@NiFe exhibits a negligible elevation of about 10 mV after 25 h short-term OWS test, showing the much higher stability than that with RuO₂ (70 mV). Moreover, the electrolytic cell with BSCF@CeO₂@NiFe (Figure 3e) also shows a slight degradation after long-term 100 h test, and the voltage of this electrolytic cell almost has no attenuation. Nevertheless, it is worth noting that, in the initial 10 h of the stability test, the electrolytic cell voltage rapidly increases until it reaches the maximum value of 1.87 V, and then sharply drops to 1.81 V in the next approximate 1 h test. The quick degradation of the electrolytic cell can be related to the corrosion of BSCF@CeO₂@NiFe in the Cl⁻-containing electrolyte and appearance of the passivation layer [3]. The subsequent performance recovery can be ascribed to be the surface amorphization of BSCF perovskite anode in the alkaline overall water splitting test [53,57] and subsequent appearance of CoFe-LDH on the BSCF surface caused by the dynamic surface self-reconstruction [52,58]. Considering the high splitting overpotential of natural seawater, the stability test of BSCF@CeO₂@NiFe in the natural seawater is performed at 10 mA cm⁻² to prevent the formation of the strong corrosive ClO⁻. Figure 3c is a corresponding seawater splitting schematic. As shown in Figure 3f, during the 200 h stability test in 1 M KOH + seawater, the variation trend of this electrolytic cell voltage is similar with that in 1 M KOH + 0.5 M NaCl, displaying a superior stability after long-term test. Compared with the initial cell voltage (1.56 V), the final cell voltage only increases by about 30 mV after 200 h. In addition, during the natural seawater test,

the anode and cathode products are collected by the drainage method and compared with their theoretical values (seeing Figure S4, Supplementary Information). The results show that the test values are basically consistent with the theoretical values, indicating that the Faraday efficiency are close to 100%, and almost no Cl_2 is produced (Figure 3g). The result indicates an excellent OER selectivity of BSCF@CeO₂@NiFe.

4. Discussion

As mentioned before, BSCF@CeO₂@NiFe shows a superior OER catalytic activity in alkaline solutions. To clarify the mechanisms, we further perform the EIS and C_{dl} measurements. It is known that ECSA of the electrocatalysts can be estimated by calculating C_{dl} from the cyclic voltammetry (CV) curves (Figure 4a–d). The C_{dl} value of BSCF@CeO₂@NiFe is 2.70 mF cm⁻² which is higher than that of NiFe-LDH (1.19 mF cm⁻²), BSCF@NiFe (1.07 mF cm⁻²) and BSCF (1.91 mF cm⁻²) (Figure 4e). The EIS Nyquist plots in Figure 4f further shows that BSCF@CeO₂@NiFe owns a lower charge-transfer resistance (R_{ct} , 2.1 Ω) compared with other samples [59], which demonstrates its quick charge transport capability and favorable OER dynamics [60]. The improvement of C_{dl} and smaller R_{ct} of BSCF@CeO₂@NiFe can be related to the introduction of CeO₂ with strong oxygen-gathering ability and heterogeneous interface formed between CeO₂ and metal (oxy)hydroxides (NiFe-LDH) [61].

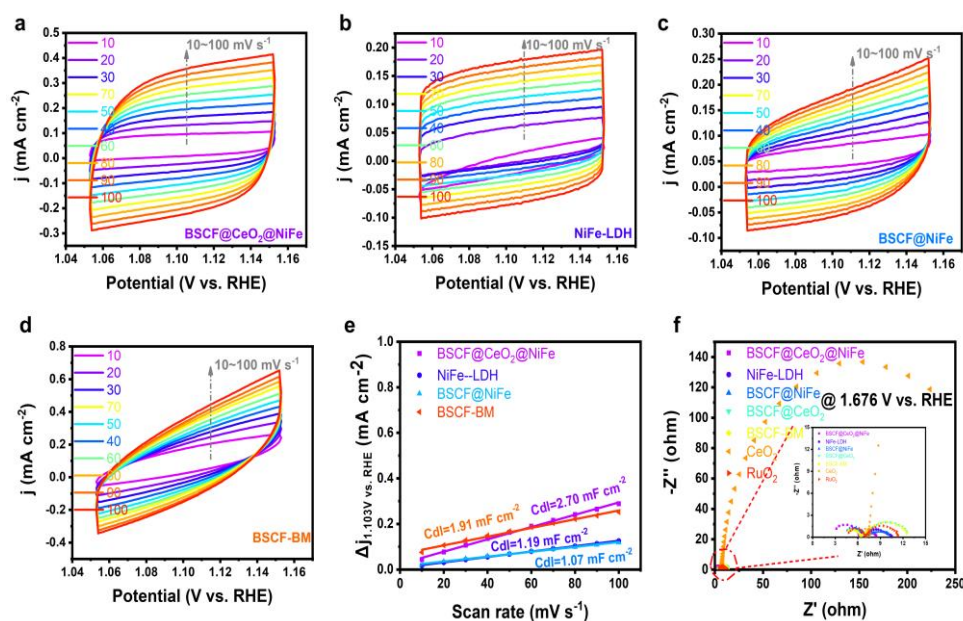


Figure 4. CV curves of BSCF@CeO₂@NiFe (a), NiFe-LDH (b), BSCF@NiFe (c), and BSCF (d) catalysts at 0.15–0.25 V (vs. Hg/HgO) with scan rates of 10, 20, 30, 40, 50, 60, 70, 80, 90, and 100 mV s⁻¹. Corresponding C_{dl} values (e) and EIS Nyquist plots (f) of BSCF@CeO₂@NiFe, BSCF@NiFe, NiFe-LDH, BSCF@CeO₂, BSCF, CeO₂, and RuO₂. The insert of (f) is the EIS plots in a smaller range.

5. Conclusions

In this work, we successfully synthesized heterostructure electrocatalyst of BSCF@CeO₂@NiFe by compositing CeO₂, NiFe-LDH with BSCF. Benefiting from its large ECSA as well as smaller charge-transfer resistance, the synthesized BSCF@CeO₂@NiFe showed a superior OER catalytic activity with $E_{j=100}$ being 1.52 V in 1 M KOH, 1.54 V in 1 M KOH + 0.5 M NaCl and 1.62 V in 1 M KOH + seawater, which were even lower than NiFe-LDH and RuO₂. Additionally, our BSCF@CeO₂@NiFe had an excellent long-term durability and self-recovery capability during the stability test.

Supplementary Materials: The following are available online at <https://www.mdpi.com/article/10.3390/pr10040668/s1>, Figure S1: HER performances comparison of BSCF and 20 wt% Pt/C. Figure S2: 10 Consecutive LSV curves of catalyst NiFe-LDH at the different measuring times. Figure S3: CV curves of (a) BSCF@CeO₂@NiFe-113 and (b) NiFe-LDH at continuous 25-cycle tests. Figure S4: Diagram of oxygen evolution Faraday Efficiency test device. Table S1: The main compositions in natural seawater. Table S2: OER performance comparison of BSCF with other perovskites. Table S3: Comparison of the OER activities of the different types of perovskite composites in this work and the other reports [62–73].

Author Contributions: Investigation, data curation, and writing of the original manuscript, R.H. and F.L.; conceptualization, investigation, methodology, supervision, and writing—review and editing, H.M.; investigation and data curation, Q.W., H.Z., F.W. and J.Y.; and data analysis, H.Q. All authors have read and agreed to the published version of the manuscript.

Funding: This research received no external funding.

Institutional Review Board Statement: Not applicable.

Informed Consent Statement: Not applicable.

Data Availability Statement: Not applicable.

Acknowledgments: The authors are grateful for the financial supports from the National Natural Science Foundation of China (Grant No. 51871126), Ningbo major special projects of the Plan “Science and Technology Innovation 2025” (Grant No. 2020Z107), Zhejiang Provincial Natural Science Foundation of China Grant (Grant No. LY21E010002) and K.C. Wong Magna Fund in Ningbo University.

Conflicts of Interest: The authors declare no conflict of interest.

References

1. Yu, L.; Zhu, Q.; Song, S.; McElhenny, B.; Wang, D.; Wu, C.; Qin, Z.; Bao, J.; Yu, Y.; Chen, S.; et al. Non-noble metal-nitride based electrocatalysts for high-performance alkaline seawater electrolysis. *Nat. Commun.* **2019**, *10*, 5106. [[CrossRef](#)] [[PubMed](#)]
2. Ma, Y.-Y.; Wu, C.-X.; Feng, X.-J.; Tan, H.-Q.; Yan, L.-K.; Liu, Y.; Kang, Z.-H.; Wang, E.-B.; Li, Y.-G. Highly efficient hydrogen evolution from seawater by a low-cost and stable CoMoP@C electrocatalyst superior to Pt/C. *Energy Environ. Sci.* **2017**, *10*, 788–798. [[CrossRef](#)]
3. Kuang, Y.; Kenney, M.J.; Meng, Y.; Hung, W.H.; Liu, Y.; Huang, J.E.; Prasanna, R.; Li, P.; Li, Y.; Wang, L.; et al. Solar-driven, highly sustained splitting of seawater into hydrogen and oxygen fuels. *Proc. Natl. Acad. Sci. USA* **2019**, *116*, 6624–6629. [[CrossRef](#)] [[PubMed](#)]
4. Morales-Guio, C.G.; Stern, L.A.; Hu, X. Nanostructured hydrotreating catalysts for electrochemical hydrogen evolution. *Chem. Soc. Rev.* **2014**, *43*, 6555–6569. [[CrossRef](#)] [[PubMed](#)]
5. Chen, G.; Wang, T.; Zhang, J.; Liu, P.; Sun, H.; Zhuang, X.; Chen, M.; Feng, X. Accelerated Hydrogen Evolution Kinetics on NiFe-Layered Double Hydroxide Electrocatalysts by Tailoring Water Dissociation Active Sites. *Adv. Mater.* **2018**, *30*, 1706279. [[CrossRef](#)] [[PubMed](#)]
6. Zhang, J.; Hu, W.; Cao, S.; Piao, L. Recent progress for hydrogen production by photocatalytic natural or simulated seawater splitting. *Nano Res.* **2020**, *13*, 2313–2322. [[CrossRef](#)]
7. Cui, B.; Hu, Z.; Liu, C.; Liu, S.; Chen, F.; Hu, S.; Zhang, J.; Zhou, W.; Deng, Y.; Qin, Z.; et al. Heterogeneous lamellar-edged Fe-Ni(OH)₂/Ni₃S₂ nanoarray for efficient and stable seawater oxidation. *Nano Res.* **2020**, *14*, 1149–1155. [[CrossRef](#)]
8. Vos, J.G.; Wezendonk, T.A.; Jeremiasse, A.W.; Koper, M.T.M. MnOx/IrOx as Selective Oxygen Evolution Electrocatalyst in Acidic Chloride Solution. *J. Am. Chem. Soc.* **2018**, *140*, 10270–10281. [[CrossRef](#)]
9. Li, B.Q.; Zhang, S.Y.; Tang, C.; Cui, X.; Zhang, Q. Anionic Regulated NiFe (Oxy)Sulfide Electrocatalysts for Water Oxidation. *Small* **2017**, *13*, 1700610. [[CrossRef](#)]
10. Li, P.; Wang, S.; Samo, I.A.; Zhang, X.; Wang, Z.; Wang, C.; Li, Y.; Du, Y.; Zhong, Y.; Cheng, C.; et al. Common-Ion Effect Triggered Highly Sustained Seawater Electrolysis with Additional NaCl Production. *Research* **2020**, *2020*, 2872141. [[CrossRef](#)]
11. Liu, G.; Xu, Y.; Yang, T.; Jiang, L. Recent advances in electrocatalysts for seawater splitting. *Nano Mater. Sci.* **2020**. [[CrossRef](#)]
12. Yao, Y.; Gao, X.; Meng, X. Recent advances on electrocatalytic and photocatalytic seawater splitting for hydrogen evolution. *Int. J. Hydrog. Energy* **2021**, *46*, 9087–9100. [[CrossRef](#)]
13. Hausmann, J.N.; Schlögl, R.; Menezes, P.W.; Driess, M. Is direct seawater splitting economically meaningful? *Energy Environ. Sci.* **2021**, *14*, 3679–3685. [[CrossRef](#)]
14. Tong, W.; Forster, M.; Dionigi, F.; Dresp, S.; Sadeghi Erami, R.; Strasser, P.; Cowan, A.J.; Farràs, P. Electrolysis of low-grade and saline surface water. *Nat. Energy* **2020**, *5*, 367–377. [[CrossRef](#)]

15. Dresp, S.; Thanh, T.N.; Klingenhof, M.; Brückner, S.; Hauke, P.; Strasser, P. Efficient direct seawater electrolyzers using selective alkaline NiFe-LDH as OER catalyst in asymmetric electrolyte feeds. *Energy Environ. Sci.* **2020**, *13*, 1725–1729. [[CrossRef](#)]
16. Barreca, D.; Carraro, G.; Gasparotto, A.; Maccato, C.; Warwick, M.E.A.; Kaunisto, K.; Sada, C.; Turner, S.; Gönüllü, Y.; Ruoko, T.-P.; et al. Fe₂O₃-TiO₂Nano-heterostructure Photoanodes for Highly Efficient Solar Water Oxidation. *Adv. Mater. Interfaces* **2015**, *2*, 1500313. [[CrossRef](#)]
17. Duan, Y.; Yu, Z.Y.; Hu, S.J.; Zheng, X.S.; Zhang, C.T.; Ding, H.H.; Hu, B.C.; Fu, Q.Q.; Yu, Z.L.; Zheng, X.; et al. Scaled-Up Synthesis of Amorphous NiFeMo Oxides and Their Rapid Surface Reconstruction for Superior Oxygen Evolution Catalysis. *Angew Chem. Int. Ed. Engl.* **2019**, *58*, 15772–15777. [[CrossRef](#)]
18. Gorlin, M.; Chernev, P.; Ferreira de Araujo, J.; Reier, T.; Dresp, S.; Paul, B.; Krahnert, R.; Dau, H.; Strasser, P. Oxygen Evolution Reaction Dynamics, Faradaic Charge Efficiency, and the Active Metal Redox States of Ni-Fe Oxide Water Splitting Electrocatalysts. *J. Am. Chem. Soc.* **2016**, *138*, 5603–5614. [[CrossRef](#)]
19. Cox, C.R.; Lee, J.Z.; Nocera, D.G.; Buonassisi, T. Ten-percent solar-to-fuel conversion with nonprecious materials. *Proc. Natl. Acad. Sci. USA* **2014**, *111*, 14057–14061. [[CrossRef](#)]
20. Oh, N.K.; Seo, J.; Lee, S.; Kim, H.J.; Kim, U.; Lee, J.; Han, Y.K.; Park, H. Highly efficient and robust noble-metal free bifunctional water electrolysis catalyst achieved via complementary charge transfer. *Nat. Commun.* **2021**, *12*, 4606. [[CrossRef](#)]
21. Tsai, H.W.; Su, Y.H. Double Perovskite LaFe_{1-x}Ni_xO₃ Coated with Sea Urchin-like Gold Nanoparticles Using Electrophoresis as the Photoelectrochemical Electrode to Enhance H₂ Production via Surface Plasmon Resonance Effect. *Nanomaterials* **2022**, *12*, 622. [[CrossRef](#)] [[PubMed](#)]
22. Nandikes, G.; Gouse Peera, S.; Singh, L. Perovskite-Based Nanocomposite Electrocatalysts: An Alternative to Platinum ORR Catalyst in Microbial Fuel Cell Cathodes. *Energies* **2022**, *15*, 272. [[CrossRef](#)]
23. Yu, L.; Wu, L.; Song, S.; McElhenny, B.; Zhang, F.; Chen, S.; Ren, Z. Hydrogen Generation from Seawater Electrolysis over a Sandwich-like NiCoN|Ni₃P|NiCoN Microsheet Array Catalyst. *ACS Energy Lett.* **2020**, *5*, 2681–2689. [[CrossRef](#)]
24. Peera, S.G.; Koutavarapu, R.; Liu, C.; Rajeshkhanna, G.; Asokan, A.; Reddy, C.V. Cobalt Nanoparticle-Embedded Nitrogen-Doped Carbon Catalyst Derived from a Solid-State Metal-Organic Framework Complex for OER and HER Electrocatalysis. *Energies* **2021**, *14*, 1320. [[CrossRef](#)]
25. Wang, P.; Qi, J.; Chen, X.; Li, C.; Li, W.; Wang, T.; Liang, C. Three-Dimensional Heterostructured NiCoP@NiMn-Layered Double Hydroxide Arrays Supported on Ni Foam as a Bifunctional Electrocatalyst for Overall Water Splitting. *ACS Appl. Mater. Interfaces* **2020**, *12*, 4385–4395. [[CrossRef](#)] [[PubMed](#)]
26. Wang, Z.; Wang, S.; Ma, L.; Guo, Y.; Sun, J.; Zhang, N.; Jiang, R. Water-Induced Formation of Ni₂P-Ni₁₂P₅ Interfaces with Superior Electrocatalytic Activity toward Hydrogen Evolution Reaction. *Small* **2021**, *17*, e2006770. [[CrossRef](#)]
27. Zou, Y.; Xiao, B.; Shi, J.-W.; Hao, H.; Ma, D.; Lv, Y.; Sun, G.; Li, J.; Cheng, Y. 3D hierarchical heterostructure assembled by NiFe LDH/(NiFe)_{Sx} on biomass-derived hollow carbon microtubes as bifunctional electrocatalysts for overall water splitting. *Electrochim. Acta* **2020**, *348*, 136339. [[CrossRef](#)]
28. Liu, C.; Ma, H.; Yuan, M.; Yu, Z.; Li, J.; Shi, K.; Liang, Z.; Yang, Y.; Zhu, T.; Sun, G.; et al. (NiFe)_{S2} nanoparticles grown on graphene as an efficient electrocatalyst for oxygen evolution reaction. *Electrochim. Acta* **2018**, *286*, 195–204. [[CrossRef](#)]
29. Zhou, W.; Wu, X.-J.; Cao, X.; Huang, X.; Tan, C.; Tian, J.; Liu, H.; Wang, J.; Zhang, H. Ni₃S₂ nanorods/Ni foam composite electrode with low overpotential for electrocatalytic oxygen evolution. *Energy Environ. Sci.* **2013**, *6*, 2921–2924. [[CrossRef](#)]
30. Wang, J.; Zhang, M.; Yang, G.; Song, W.; Zhong, W.; Wang, X.; Wang, M.; Sun, T.; Tang, Y. Heterogeneous Bimetallic Mo-Ni_{Px}/Ni_{Sy} as a Highly Efficient Electrocatalyst for Robust Overall Water Splitting. *Adv. Funct. Mater.* **2021**, *31*, 2101532. [[CrossRef](#)]
31. Dionigi, F.; Strasser, P. NiFe-Based (Oxy)hydroxide Catalysts for Oxygen Evolution Reaction in Non-Acidic Electrolytes. *Adv. Energy Mater.* **2016**, *6*, 1600621. [[CrossRef](#)]
32. Cheng, F.; Feng, X.; Chen, X.; Lin, W.; Rong, J.; Yang, W. Synergistic action of Co-Fe layered double hydroxide electrocatalyst and multiple ions of sea salt for efficient seawater oxidation at near-neutral pH. *Electrochim. Acta* **2017**, *251*, 336–343. [[CrossRef](#)]
33. Cao, S.; Huang, H.; Shi, K.; Wei, L.; You, N.; Fan, X.; Yang, Z.; Zhang, W. Engineering superhydrophilic/superaerophobic hierarchical structures of Co-CH@NiFe-LDH/NF to boost the oxygen evolution reaction. *Chem. Eng. J.* **2021**, *422*, 130123. [[CrossRef](#)]
34. Hunter, B.M.; Hieringer, W.; Winkler, J.R.; Gray, H.B.; Müller, A.M. Effect of interlayer anions on [NiFe]-LDH nanosheet water oxidation activity. *Energy Environ. Sci.* **2016**, *9*, 1734–1743. [[CrossRef](#)]
35. Andronescu, C.; Seisel, S.; Wilde, P.; Barwe, S.; Masa, J.; Chen, Y.T.; Ventosa, E.; Schuhmann, W. Influence of Temperature and Electrolyte Concentration on the Structure and Catalytic Oxygen Evolution Activity of Nickel-Iron Layered Double Hydroxide. *Chemistry* **2018**, *24*, 13773–13777. [[CrossRef](#)] [[PubMed](#)]
36. Peng, L.; Yang, N.; Yang, Y.; Wang, Q.; Xie, X.; Sun-Waterhouse, D.; Shang, L.; Zhang, T.; Waterhouse, G.I.N. Atomic Cation-Vacancy Engineering of NiFe-Layered Double Hydroxides for Improved Activity and Stability towards the Oxygen Evolution Reaction. *Angew Chem. Int. Ed. Engl.* **2021**, *60*, 24612–24619. [[CrossRef](#)]
37. Dai, J.; Zhu, Y.; Tahini, H.A.; Lin, Q.; Chen, Y.; Guan, D.; Zhou, C.; Hu, Z.; Lin, H.J.; Chan, T.S.; et al. Single-phase perovskite oxide with super-exchange induced atomic-scale synergistic active centers enables ultrafast hydrogen evolution. *Nat. Commun.* **2020**, *11*, 5657. [[CrossRef](#)]

38. Guan, D.; Ryu, G.; Hu, Z.; Zhou, J.; Dong, C.L.; Huang, Y.C.; Zhang, K.; Zhong, Y.; Komarek, A.C.; Zhu, M.; et al. Utilizing ion leaching effects for achieving high oxygen-evolving performance on hybrid nanocomposite with self-optimized behaviors. *Nat. Commun.* **2020**, *11*, 3376. [[CrossRef](#)]
39. She, S.; Zhu, Y.; Tahini, H.A.; Wu, X.; Guan, D.; Chen, Y.; Dai, J.; Chen, Y.; Tang, W.; Smith, S.C.; et al. Efficient Water Splitting Actualized through an Electrochemistry-Induced Hetero-Structured Antiperovskite/(Oxy)Hydroxide Hybrid. *Small* **2020**, *16*, e2006800. [[CrossRef](#)]
40. Wu, X.; Miao, H.; Yin, M.; Hu, R.; Wang, F.; Zhang, H.; Xia, L.; Zhang, C.; Yuan, J. Biomimetic construction of bifunctional perovskite oxygen catalyst for zinc-air batteries. *Electrochim. Acta* **2021**, *399*, 139407. [[CrossRef](#)]
41. Li, G.; Hou, S.; Gui, L.; Feng, F.; Zhang, D.; He, B.; Zhao, L. Carbon quantum dots decorated Ba_{0.5}Sr_{0.5}Co_{0.8}Fe_{0.2}O₃- perovskite nanofibers for boosting oxygen evolution reaction. *Appl. Catal. B Environ.* **2019**, *257*, 117919. [[CrossRef](#)]
42. Dai, Y.; Yu, J.; Zhang, Z.; Cheng, C.; Tan, P.; Shao, Z.; Ni, M. Interfacial La Diffusion in the CeO₂/LaFeO₃ Hybrid for Enhanced Oxygen Evolution Activity. *ACS Appl. Mater. Interfaces* **2021**, *13*, 2799–2806. [[CrossRef](#)] [[PubMed](#)]
43. Liang, F.; Yu, Y.; Zhou, W.; Xu, X.; Zhu, Z. Highly defective CeO₂ as a promoter for efficient and stable water oxidation. *J. Mater. Chem. A* **2015**, *3*, 634–640. [[CrossRef](#)]
44. Wang, X.; Yan, H.; Zhang, J.; Hong, X.; Yang, S.; Wang, C.; Li, Z. Stamen-petal-like CeO₂/NiMn layered double hydroxides composite for high-rate-performance supercapacitor. *J. Alloy Compd.* **2019**, *810*, 151911. [[CrossRef](#)]
45. Xiao, Y.; Li, H.; Xie, K. Activating Lattice Oxygen at the Twisted Surface in a Mesoporous CeO₂ Single Crystal for Efficient and Durable Catalytic CO Oxidation. *Angew. Chem. Int. Ed. Engl.* **2021**, *60*, 5240–5244. [[CrossRef](#)]
46. Wu, X.; Miao, H.; Hu, R.; Chen, B.; Yin, M.; Zhang, H.; Xia, L.; Zhang, C.; Yuan, J. A-site deficient perovskite nanofibers boost oxygen evolution reaction for zinc-air batteries. *Appl. Surf. Sci.* **2021**, *536*, 147806. [[CrossRef](#)]
47. Zhao, Y.; Li, F.; Zhang, R.; Evans, D.G.; Duan, X. Preparation of Layered Double-Hydroxide Nanomaterials with a Uniform Crystallite Size Using a New Method Involving Separate Nucleation and Aging Steps. *Chem. Mater.* **2002**, *14*, 4286–4291. [[CrossRef](#)]
48. Xue, X.; Yu, F.; Peng, B.; Wang, G.; Lv, Y.; Chen, L.; Yao, Y.; Dai, B.; Shi, Y.; Guo, X. One-step synthesis of nickel–iron layered double hydroxides with tungstate acid anions via flash nano-precipitation for the oxygen evolution reaction. *Sustain. Energy Fuels* **2019**, *3*, 237–244. [[CrossRef](#)]
49. Miao, H.; Chen, B.; Li, S.; Wu, X.; Wang, Q.; Zhang, C.; Sun, Z.; Li, H. All-solid-state flexible zinc-air battery with polyacrylamide alkaline gel electrolyte. *J. Power Sources* **2020**, *450*, 227653. [[CrossRef](#)]
50. Han, Q.; Luo, Y.; Li, J.; Du, X.; Sun, S.; Wang, Y.; Liu, G.; Chen, Z. Efficient NiFe-based Oxygen Evolution Electrocatalysts and Origin of their Distinct Activity. *Appl. Catal. B Environ.* **2021**, *304*, 120937. [[CrossRef](#)]
51. Dresp, S.; Dionigi, F.; Klingenhof, M.; Strasser, P. Direct Electrolytic Splitting of Seawater: Opportunities and Challenges. *ACS Energy Lett.* **2019**, *4*, 933–942. [[CrossRef](#)]
52. Fabbri, E.; Nachttegaal, M.; Binnering, T.; Cheng, X.; Kim, B.J.; Durst, J.; Bozza, F.; Graule, T.; Schaublin, R.; Wiles, L.; et al. Dynamic surface self-reconstruction is the key of highly active perovskite nano-electrocatalysts for water splitting. *Nat. Mater.* **2017**, *16*, 925–931. [[CrossRef](#)] [[PubMed](#)]
53. Risch, M.; Grimaud, A.; May, K.J.; Stoerzinger, K.A.; Chen, T.J.; Mansour, A.N.; Shao-Horn, Y. Structural Changes of Cobalt-Based Perovskites upon Water Oxidation Investigated by EXAFS. *J. Phys. Chem. C* **2013**, *117*, 8628–8635. [[CrossRef](#)]
54. Majee, R.; Islam, Q.A.; Bhattacharyya, S. Surface Charge Modulation of Perovskite Oxides at the Crystalline Junction with Layered Double Hydroxide for a Durable Rechargeable Zinc-Air Battery. *ACS Appl. Mater. Interfaces* **2019**, *11*, 35853–35862. [[CrossRef](#)]
55. Zhu, Y.; Zhou, W.; Chen, Z.G.; Chen, Y.; Su, C.; Tade, M.O.; Shao, Z. SrNb_(0.1)Co_(0.7)Fe_(0.2)O_(3-δ) perovskite as a next-generation electrocatalyst for oxygen evolution in alkaline solution. *Angew Chem. Int. Ed. Engl.* **2015**, *54*, 3897–3901. [[CrossRef](#)]
56. Cheng, X.; Fabbri, E.; Kim, B.; Nachttegaal, M.; Schmidt, T.J. Effect of ball milling on the electrocatalytic activity of Ba_{0.5}Sr_{0.5}Co_{0.8}Fe_{0.2}O₃ towards the oxygen evolution reaction. *J. Mater. Chem. A* **2017**, *5*, 13130–13137. [[CrossRef](#)]
57. May, K.J.; Carlton, C.E.; Stoerzinger, K.A.; Risch, M.; Suntivich, J.; Lee, Y.-L.; Grimaud, A.; Shao-Horn, Y. Influence of Oxygen Evolution during Water Oxidation on the Surface of Perovskite Oxide Catalysts. *J. Phys. Chem. Lett.* **2012**, *3*, 3264–3270. [[CrossRef](#)]
58. Shen, T.H.; Spillane, L.; Vavra, J.; Pham, T.H.M.; Peng, J.; Shao-Horn, Y.; Tileli, V. Oxygen Evolution Reaction in Ba_{0.5}Sr_{0.5}Co_{0.8}Fe_{0.2}O_{3-δ} Aided by Intrinsic Co/Fe Spinel-Like Surface. *J. Am. Chem. Soc.* **2020**, *142*, 15876–15883. [[CrossRef](#)]
59. Zhu, Y.; Zhou, W.; Zhong, Y.; Bu, Y.; Chen, X.; Zhong, Q.; Liu, M.; Shao, Z. A Perovskite Nanorod as Bifunctional Electrocatalyst for Overall Water Splitting. *Adv. Energy Mater.* **2017**, *7*, 1602122. [[CrossRef](#)]
60. Yu, L.; Wu, L.; McElhenny, B.; Song, S.; Luo, D.; Zhang, F.; Yu, Y.; Chen, S.; Ren, Z. Ultrafast room-temperature synthesis of porous S-doped Ni/Fe (oxy)hydroxide electrodes for oxygen evolution catalysis in seawater splitting. *Energy Environ. Sci.* **2020**, *13*, 3439–3446. [[CrossRef](#)]
61. Li, Y.; Luo, W.; Wu, D.; Wang, Q.; Yin, J.; Xi, P.; Qu, Y.; Gu, M.; Zhang, X.; Lu, Z. Atomic-level correlation between the electrochemical performance of an oxygen-evolving catalyst and the effects of CeO₂ functionalization. *Nano Res.* **2021**, 1–7. [[CrossRef](#)]
62. Kim, N.-I.; Cho, S.-H.; Park, S.H.; Lee, Y.J.; Afzal, R.A.; Yoo, J.; Seo, Y.-S.; Lee, Y.J.; Park, J.-Y. B-site doping effects of NdBa_{0.75}Ca_{0.25}Co₂O_{5+δ} double perovskite catalysts for oxygen evolution and reduction reactions. *J. Mater. Chem. A* **2018**, *6*, 17807–17818. [[CrossRef](#)]

63. Ye, X.; Song, S.; Li, L.; Chang, Y.-C.; Qin, S.; Liu, Z.; Huang, Y.-C.; Zhou, J.; Zhang, L.-j.; Dong, C.-L.; et al. A'-B Intersite Cooperation-Enhanced Water Splitting in Quadruple Perovskite Oxide CaCu₃Ir₄O₁₂. *Chem. Mater.* **2021**, *33*, 9295–9305. [[CrossRef](#)]
64. Li, X.; Wang, H.; Cui, Z.; Li, Y.; Xin, S.; Zhou, J.; Long, Y.; Jin, C.; Goodenough, J.B. Exceptional oxygen evolution reactivities on CaCoO₃ and SrCoO₃. *Sci. Adv.* **2019**, *5*, eaav6262. [[CrossRef](#)] [[PubMed](#)]
65. Yan, J.; Xia, M.; Zhu, C.; Chen, D.; Du, F. Perovskite With Tunable Active-Sites Oxidation State by High-Valence W for Enhanced Oxygen Evolution Reaction. *Front. Chem.* **2021**, *9*, 809111. [[CrossRef](#)]
66. Xiong, J.; Zhong, H.; Li, J.; Zhang, X.; Shi, J.; Cai, W.; Qu, K.; Zhu, C.; Yang, Z.; Beckman, S.P.; et al. Engineering highly active oxygen sites in perovskite oxides for stable and efficient oxygen evolution. *Appl. Catal. B Environ.* **2019**, *256*. [[CrossRef](#)]
67. Long, J.; Zhang, J.; Xu, X.; Wang, F. Crystalline NiFe layered double hydroxide with large pore volume as oxygen evolution electrocatalysts. *Mater. Chem. Phys.* **2020**, *254*, 123496. [[CrossRef](#)]
68. Mondal, S.; Majee, R.; Arif Islam, Q.; Bhattacharyya, S. 2D Heterojunction Between Double Perovskite Oxide Nanosheet and Layered Double Hydroxide to Promote Rechargeable Zinc-Air Battery Performance. *ChemElectroChem* **2020**, *7*, 5005–5012. [[CrossRef](#)]
69. Göl, E.Y.; Aytakin, A.; Özkahraman, E.E.; Karabudak, E. Investigation of oxygen evolution reaction performance of silver doped Ba_{0.5}Sr_{0.5}Co_{0.8}Fe_{0.2}O_{3-δ} perovskite structure. *J. Appl. Electrochem.* **2020**, *50*, 1037–1043. [[CrossRef](#)]
70. Zhu, Y.; Chen, G.; Zhong, Y.; Chen, Y.; Ma, N.; Zhou, W.; Shao, Z. A surface-modified antiperovskite as an electrocatalyst for water oxidation. *Nat. Commun.* **2018**, *9*, 2326. [[CrossRef](#)]
71. Tang, D.; Liu, J.; Wu, X.; Liu, R.; Han, X.; Han, Y.; Huang, H.; Liu, Y.; Kang, Z. Carbon quantum dot/NiFe layered double-hydroxide composite as a highly efficient electrocatalyst for water oxidation. *ACS Appl. Mater. Interfaces* **2014**, *6*, 7918–7925. [[CrossRef](#)] [[PubMed](#)]
72. Hua, B.; Li, M.; Zhang, Y.-Q.; Sun, Y.-F.; Luo, J.-L. All-In-One Perovskite Catalyst: Smart Controls of Architecture and Composition toward Enhanced Oxygen/Hydrogen Evolution Reactions. *Adv. Energy Mater.* **2017**, *7*, 1700666. [[CrossRef](#)]
73. Chen, G.; Zhu, Y.; Chen, H.M.; Hu, Z.; Hung, S.F.; Ma, N.; Dai, J.; Lin, H.J.; Chen, C.T.; Zhou, W.; et al. An Amorphous Nickel-Iron-Based Electrocatalyst with Unusual Local Structures for Ultrafast Oxygen Evolution Reaction. *Adv. Mater.* **2019**, *31*, e1900883. [[CrossRef](#)] [[PubMed](#)]